Standardised TruAI automated quantification of intracellular neuromelanin granules in human brain tissue sections

Anastasia Filimontseva[1,2*] ORCID 0000-0002-3316-9035 Email afil9180@uni.sydney.edu.au

Thais Cuadros[2,3*] ORCID 0000-0001-7376-7470 email thais.cuadros@vhir.org

Zac Chatterton[1,2] ORCID 0000-0002-6683-1400 email zac.chatterton@sycney.edu.au

Joan Compte[3] ORCID 0000-0001-5447-5122 email joancbf@gmail.com

YuHong Fu[1,2] ORCID 0000-0003-4539-2039 email yuhong.fu@sydney.edu.au

Miquel Vila[2,3,4,5#] ORCID 0000-0002-1352-989X email miquel.vila@vhir.org

Glenda M Halliday[1,2,#] ORCID 0000-0003-0422-8398 email glenda.halliday@sydney.edu.au

[1]The University of Sydney Brain and Mind Centre & Faculty of Medicine and Health School of Medical Sciences, Sydney, NSW 2050, Australia

[2]Aligning Science Across Parkinson's (ASAP) Collaborative Research Network, Chevy Chase, MD, 20815

[3]Neurodegenerative Diseases Research Group, Vall d'Hebron Research Institute (VHIR)-Network Center for Biomedical Research in Neurodegenerative Diseases (CIBERNED); 08035 Barcelona, Spain

[4]Department of Biochemistry and Molecular Biology, Institute of Neuroscience, Autonomous University of Barcelona; 08193 Barcelona, Spain

[5]Catalan Institution for Research and Advanced Studies (ICREA); 08010 Barcelona, Spain

*Co-first authors

[#]Corresponding authors: Professor Glenda Halliday, University of Sydney Brain and Mind Centre, 97 Church Street, Camperdown, NSW 2050 AUSTRALIA, Email: glenda.halliday@sydney.edu.au, Tel: +61 2 9351 0888 & Professor Miquel Vila, Neurodegenerative Diseases Research Group, Vall d'Hebron Research Institute (VHIR)-Network Center for Biomedical Research in Neurodegenerative Diseases (CIBERNED); 08035 Barcelona, SPAIN, Email: miquel.vila@vhir.org

Running title: Quantifying neuromelanin in brain sections

Number of text words: 3,659

Number of figures: 6 plus 3 supporting figures and 1 supporting table

Acknowledgements

The authors acknowledge: Microscopy Australia at the Sydney Microscopy and Microanalysis facility, University of Sydney, enabled by NCRIS; the Sydney Brain Bank in Australia, the Neurological Tissue BioBank at *IDIBAPS-Hospital Clínic* Barcelona and Biobank at IMIB-Instituto Murciano de Investigación Biosanitaria Pascual Parrilla Murcia in Spain, for human sample procurement; the ICTS-NANBIOSIS, U20/FVPR at VHIR, for assistance in histological processing; Heidi Cartwright for assistance with the figures.

Data availability

The data, code, protocols, training images and key lab materials used and generated in this study are listed in a Key Resource Table alongside their persistent identifiers at Zenodo DOI 10.5281/zenodo.14523067. Data and software information is also available at: 10.5281/zenodo.10494622, 10.5281/zenodo.14523067 and 10.5281/zenodo.14166452.

Funding

This work was supported in part by Aligning Science Across Parkinson's [020505] through the Michael J. Fox Foundation for Parkinson's Research (MJFF) and also by funding from the National Health and Medical Research Council of Australia to GMH [Investigator Grant 1176607]. For open access, the authors have applied a CC BY public copyright license to all Author Accepted Manuscripts arising from this submission.

Conflict of interest statement

The authors have no conflicts of interest to declare.

Ethics Approval

Tissue was obtained from three brain banks, the Sydney Brain Bank in Australia and the Neurological Tissue BioBank at *IDIBAPS-Hospital Clínic* Barcelona and Biobank at IMIB-Instituto Murciano de Investigación Biosanitaria Pascual Parrilla Murcia in Spain. These brain banks are ethically established for the collection of human postmortem brains for research purposes under Australian (Human Tissue Act 1983 No 164) and Spanish (233/2044)

regulations using established guidelines (CPMP/ICH/135/95). The study was approved by the University of Sydney Human Research Ethics Committee (2021/845) and the Vall d'Hebron Research Institute (VHIR) Ethical Clinical Investigation Committee (PR (AG) 370/2014).

Key points

- Standardised, reliable TruAI automated quantitation of intracellular neuromelanin granules in human brain sections gives novel insights into their structure and function
- extracellular neuromelanin granules, released from dying pigmented neurons, are significantly smaller than intracellular neuromelanin granules
- intracellular neuromelanin granules change their properties with healthy ageing becoming darker, consistent with more antioxidant eumelanin

Abstract

Aims: To standardise and automate the quantitation of human-unique neuromelanin granules in catecholamine neurons in post-mortem tissue sections from healthy individuals at different ages to understand any changes in these granules with age.

Methods: 5-6µm thick fixed and paraffin-embedded transverse midbrain tissue sections were supplied from 47 cases from three brain banks following ethics approvals. Sections were prepared and automated digital images acquired. Standardisation and automation of the quantification of neuromelanin granules was performed using the TruAI feature of the Olympus VS200 desktop platform. Comparisons between stained and unstained sections as well as correlations with age were performed.

Results: The automated platform reliably identified both stained and unstained intracellular and extracellular neuromelanin granules, showing high reproducibility in measurements across laboratories using different tissue processing methods. Extracellular neuromelanin granules were significantly smaller than intracellular neuromelanin granules. Sections processed for hematoxylin and eosin staining impacted on size and colour of both neuromelanin and the neurons containing neuromelanin. Hematoxylin made neuromelanin bluer and the increased

tissue processing made the intracellular area occupied by neuromelanin smaller in younger people. There was an increase in neuromelanin optical density and colour change (more brown) with age.

Conclusions: The TruAI automated platform reliably quantifies individual neuromelanin granules in catecholamine neurons. Extracellular neuromelanin is considerably smaller in size than intracellular neuromelanin, and intracellular neuromelanin changes its properties with age. The darkening and colour change of intracellular neuromelanin suggests an increase in eumelanin over time in healthy individuals. These changes can be reliably identified using the automated platform.

Key words: artificial intelligence automation, computer-assisted quantitation, colour identification, extracellular neuromelanin, intracellular neuromelanin, optical density

List of abbreviations

AI	artificial intelligence	ROI	region of interest
eNM	extracellular neuromelanin	SND	substantia nigra pars compacta, dorsal tier
H&E	Hematoxylin and Eosin	SNL	substantia nigra pars compacta, lateral part
iNM	intracellular neuromelanin	SNpc	substantia nigra pars compacta
PD	Parkinson's disease	SNV	substantia nigra pars compacta, ventral tier

Introduction

Artificial intelligence (AI) is now frequently used to objectively analyse diverse images and has transformed many medical analyses by providing diagnostic and pathological classifications [1-3]. Such AI platforms provide more efficient and objective outcomes to the traditional manual scoring or counting methods previously used, saving time and improving accuracy in classifications and other analyses. Many public bioimaging repositories now have

open-source semi-automated AI quantification platforms and workflows readily available [4-6]. Despite these advances, there are limitations in these quantification workflows for particular types of analyses. For example, some automated analyses are only applicable to small regions of interest (ROIs) [1]. This is inconvenient because whole-slide/image analyses are necessary for understanding pathological disease mechanisms, especially in neurodegenerative research. Additionally, publicly shared deep learning algorithms are streamlined for overall general use rather than assessment of specialized cellular organelles. This maximises reproducibility across diverse types of studies but user-friendly protocols for the analysis of these more specific cellular features also need development.

Human catecholaminergic neurons contain a unique intracellular pigment – neuromelanin granules – which begin to accumulate at around 3-5 years of age and are fully developed between 20 and 50 years of age [7]. These neurons are selectively vulnerable to Parkinson's disease (PD), the second most common neurodegenerative disorder that manifests in motor and non-motor symptoms usually in late adulthood [8]. These symptoms arise due to gradient depigmentation and loss of catecholaminergic neurons in the substantia nigra pars compacta (SNpc), locus coeruleus and ventral tegmental area [8, 9]. Cell vulnerability is associated with neuromelanin accumulation, but the exact contribution of this macromolecule in PD remains unclear due to the time-consuming quantitation required across several anatomical regions in large-sized human post-mortem sections, and the lack of endogenous neuromelanin in catecholaminergic neurons in rodent or primate models. Despite this, the role of neuromelanin in cell pathogenesis has been investigated at the regional level by quantifying the number of pigmented cells in catecholaminergic regions [8, 10] and more recently by measuring the optical density of intracellular neuromelanin granules (iNM) [11-14]. However, due to different histological preparations of sections and the use of different optical density measurements,

iNM analyses have not been standardized and a high-capability analysis platform is needed for more robust, reproducible and efficient analyses.

We present an automated image acquisition and quantification protocol for iNM analyses in human post-mortem sections. The platform can be used on digital images of unstained or hematoxylin and eosin (H&E) stained tissue by applying the AI trained automated quantification of neuromelanin using the Olympus VS200 desktop technology (EVIDENT Technology GmbH, ver. 4.1.1 build 29408). The platform allows the quantification of the size, optical density and intracellular area occupied by iNM in these histological preparations, and also the quantification of previously unexplored red, green and blue colour features of iNM. This is the first platform for the automated standardized analysis of iNM in human brain sections and it has revealed surprising significant differences in the size of neuromelanin granules as well as identified potential histological processing effects that impact on age associations.

Materials and Methods

The platform and workflow are presented in Figure 1. Briefly, tissue is processed and formalin-fixed paraffin-embedded sections are prepared for H&E staining, or are kept unstained. For automated digital image acquisition, we used the Slide Scanner (SLIDEVIEW VS200, Tokyo, Japan). To automate the quantification of iNM, we used the TruAI feature of the Olympus VS200 desktop technology (EVIDENT Technology GmbH, ver. 4.1.1 build 29408, https://evidentscientific.com/en/software).

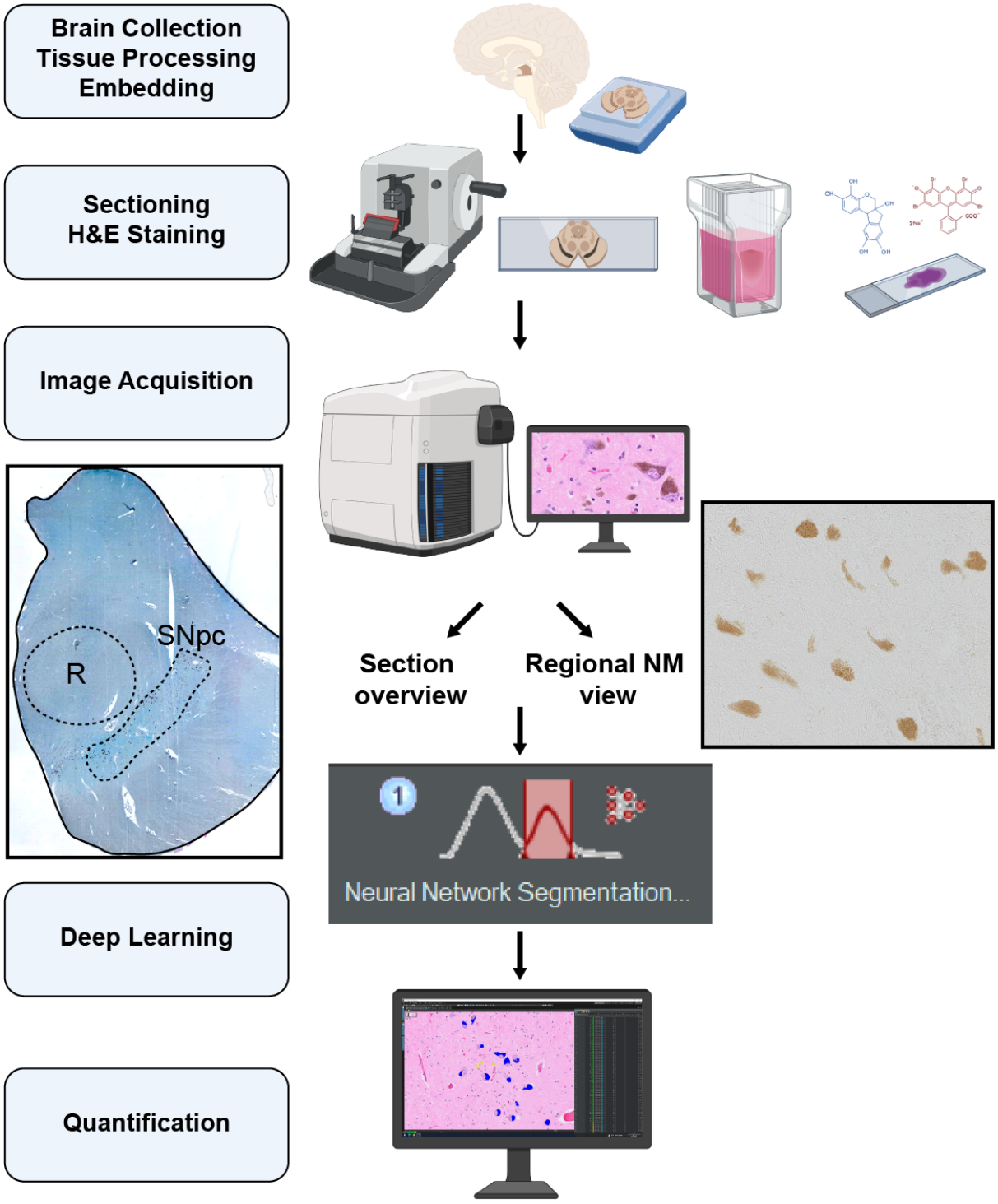

Figure 1 *Platform and workflow for neuromelanin granule (NM) automatic quantification. Brain samples are collected and undergo standard processing procedures. After sectioning, images are acquired by scanning the slides. Anatomical delineations of neuromelanin-containing regions (such as the substantia nigra pars compacta, SNpc) and nearby landmarks (such as red nucleus, R) are identified. Lastly, standardized features of intracellular neuromelanin are determined by applying the AI trained automated quantification protocol.*

Case selection and tissue processing

Five to six µm transverse brainstem sections through the midbrain at the level of the red nucleus were provided by three ethically approved brain banks (see ethics approvals) from 21 healthy control cases aged from 21 to 100 years old (used for healthy age related studies) and 26 additional cases overlapping in age but with neurological disease (used for maximizing and validating the cutoff for extracellular neuromelanin from dying cells). Case information and section use is given in the table in the supporting information. Sections were deparaffinized by incubation at 60°C for 30 min to 1 hr.

To assess unstained neuromelanin granules, sections were submerged in HistoChoice Clearing Agent (Sigma-Aldrich, H2779) for 2 x 7 min, followed by rehydration in decreasing ethanol concentrations (100% ethanol for 2 x 3 min, 95% ethanol for 3 min, 70% ethanol for 3 min) and distilled H_2O for 3 min. Slides were submerged in phosphate-buffered saline and coverslipped using a Fluorescence Mounting Medium (DAKO, S302380-2) for imaging.

To assess H&E stained iNM granules, sections were submerged in xylene for 3 x 3 min and rehydrated in decreasing ethanol concentrations (100% ethanol for 2 x 5 min, 95% ethanol for 2 x 5 min, 70% ethanol for 2 x 5 min) and double distilled H_2O for 5 min. Sections were stained with Harris' Hematoxylin solution for 2 min and rinsed for 5 min under running tap water, then 0.1% Eosin for 2 min, washed by dipping in water, and differentiated in 70% ethanol for 3 min. Sections were dehydrated in increasing ethanol concentrations (96% ethanol for 3 min, 100% ethanol for 2 x 5 min) xylene for 2 x 5 min. Sections were mounted in DPX organic mounting media.

Image acquisition

Digital images were acquired with an automated slide scanner (SLIDEVIEW VS200, Tokyo, Japan) using pre-set focusing and exposure parameters. Sections were loaded into slide trays

with edges firmly pressed against the section slots. Brightfield images were captured using a 20x X Line™ extended apochromat objective (UPLXAPO20X) which has an extended range of chromatic aberration compensation from 400 nm to 1000 nm. A focus map was generated for each sample using the semi-automatic autofocus function to optimize scan speed. Images were captured as a single image z-stack or an extended focal imaging scan, which merges multiple z-planes into a single sharp image. To ensure acquisition consistency, a "neuromelanin brightfield" scan project was created with the following steps:

1. The brightfield observation type and method were selected. The overview scan was performed at a 2x objective (NA=0.06), and the exposure was set to 295.57 µs. The first slide was manually observed and focused. All subsequent slides used this z-position as the focus depth (approximately -70um to -85um) (supporting information Figure S1a).

2. In the detail tab, a 20x objective (NA=0.8) was selected. The z-plane was set as 'Normal', and the exposure settings remained unchanged (supporting information Figure S1b).

3. 'Prefocus' was selected as the 'focus method', and 'normal' was selected as the 'focus position density' (supporting information Figure S1c).

4. In the 'Naming and Saving' window, 'multi-layer image' was selected to ensure the overview and detailed scans were saved as one file (supporting information Figure S1d1). This scan project can now be saved and applied as a single or batch scan (supporting information Figure 1d2). After the overview scan is complete, the 'scan areas' and 'focus map' can be adjusted to optimise the quality of the 20x scan (supporting information Figure S1e). Scan times vary based on sample size, objective, and modality. For example, a single plane of a 15 mm × 15 mm brightfield tissue section

at 20x takes approximately 1 minute and 45 seconds for overview, focusing, and detailed scanning.

TruAI training and automation

TruAI software training

To train the software to automatically identify neuromelanin, two automated approaches were used. The first approach assessed unstained neuromelanin and the second approach assessed manually H&E-stained iNM and extracellular NM (eNM) granules. Neuromelanin training was performed as indicated below:

1. Open a scanned neuromelanin image in the Olympus VS200 desktop software (EVIDENT Technology GmbH, ver. 4.1.1 build 29408). In the 'Detect' tab in the top right-hand corner, select 'Training Labels' and create a new foreground class in level 1.
2. For unstained neuromelanin, name this class 'neuromelanin' and keep the 'Individual Objects' option unchecked (Figure 2a).
3. For H&E-stained neuromelanin three foreground training classes were created in level 1. These classes were 'iNM', 'eNM' and 'cells without pigment'.
4. It is essential to apply the same training label to each micrograph used for neural training. To ensure this, save the label to be used for neuromelanin training later (Figure 2b).
5. Select the automatically created 'background' class and draw a continuous area using the fill icon in the bottom left-hand corner under the 'Training Labels' section (Figure 2c).

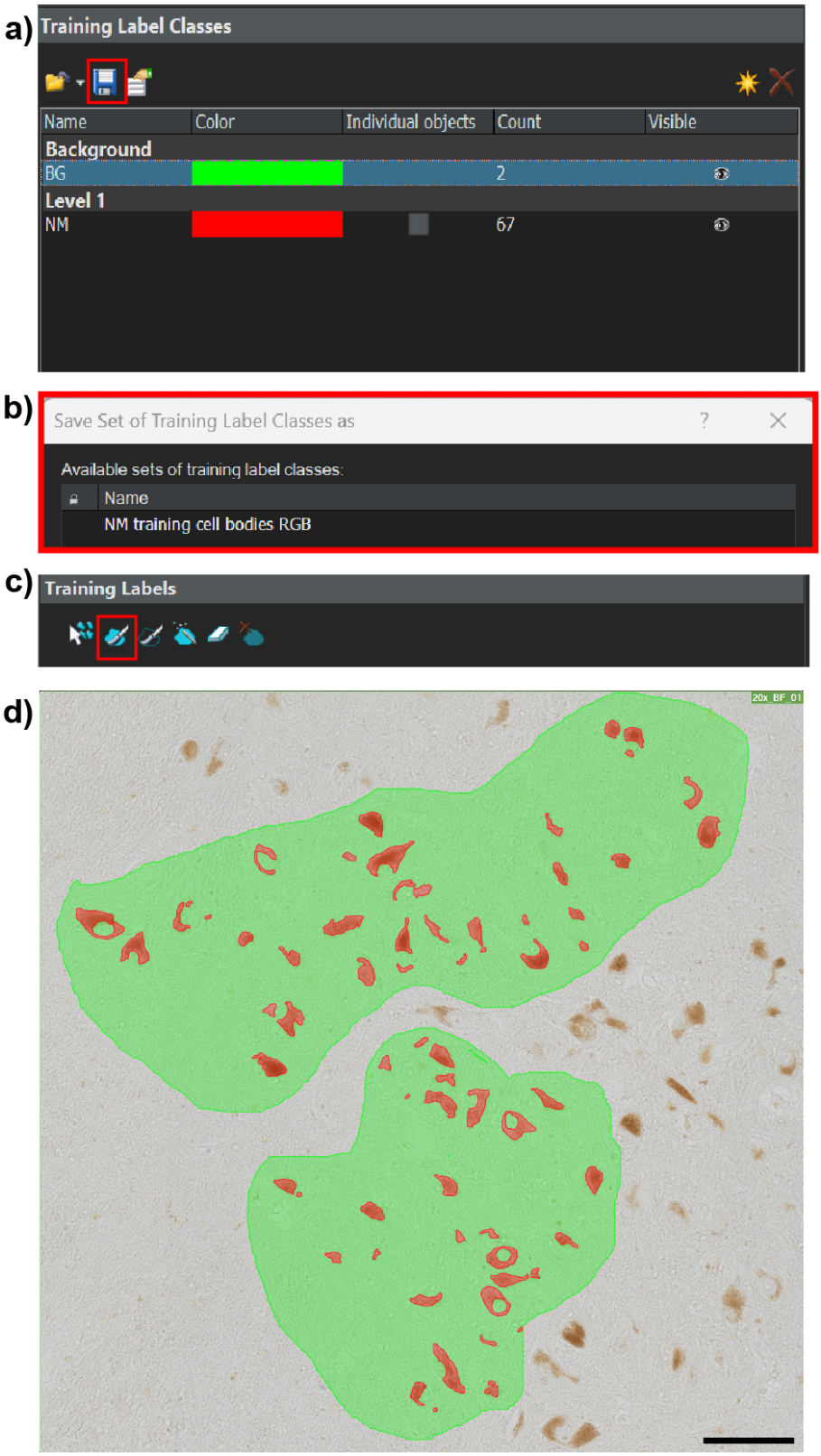

Figure 2 Training labels for neuromelanin (NM) quantification. a) Creation of a new training label class for NM granules. b) This training label must be saved and applied to sections. c) NM granules need to be accurately traced with the brush tool. d) Annotations need to be applied to 5-10 sections. Scale bar equals 100 µm.

6. Click on the ‘neuromelanin’ class and draw each neuromelanin granule in the highlighted background area. The thickness of the fill tool can be minimised to accurately outline the granules. Every neuromelanin granule must be drawn in the selected area (Figure 2d).

7. Apply steps 1-6 to 5-10 scanned sections and save them as training label images. These images were used for TruAI deep learning.

<u>TruAI deep learning automation</u>

Once at least five sections are annotated, the deep learning training can begin.

1. In the ‘Deep Learning’ tab, click ‘New Training’ and select the ‘Image Segmentation’ option. In the ‘New Training: Input and Output’ pop-up window, name the session ‘Neuromelanin Neural Training’ and load the sections with training labels by clicking the plus icon under the ‘Images’ section. Ensure that ‘basic mode’ is selected, and the input channel is red, green and blue. The individual objects option under training label classes should be left unchecked (supporting information Figure S2a).

2. In the next window select ‘Specific Network (red, green and blue)’ (supporting information Figure S2b). The required accuracy for automating neuromelanin quantitation is at least 0.85 similarity. For the first attempt, ‘no limit’ can be selected under training duration to allow for any modifications during the neural training.

3. Click ‘Start’ to commence training.

4. To increase the accuracy of neural training algorithm, more sections should be annotated (refer to TruAI software training above).

5. Select the most successful training algorithm by choosing the checkpoint with the highest similarity. Name this algorithm, provide a brief description, and save this neural

network algorithm (supporting information Figure S2c). This algorithm will be used for all future automated quantification of neuromelanin.

Fully automated TruAI quantification

This neural network algorithm can now be applied to all scanned images for automated quantification of neuromelanin.

1. In the 'Detect' window of a scanned section, select the 'Count and Measure' tab in the bottom left corner. Click on the 'Count and Measure' drop-down menu (Figure 3a1) and select 'New ROI' to draw regions on the sections (Figure 3a2).

2. Once all ROIs have been completed, click 'Neural Network Segmentation' (Figure 3b1). Load the saved neuromelanin neural network and proceed to 'Count and Measure on ROI'. Click on the 'Dimension Selector' tab to ensure this quantification is performed on the brightfield scan layer. The identified neuromelanin will be highlighted on the image (Figure 3b2).

3. The results for each individual neuromelanin granule will appear in the 'Count and Measure Results' (Figure 3c1). The parameters of interest can be chosen by clicking 'Select Object Measurements'. For analysing iNM, size, intracellular area occupied by iNM and mean red, green and blue intensities can be selected from the drop-down menu (Figure 3c2).

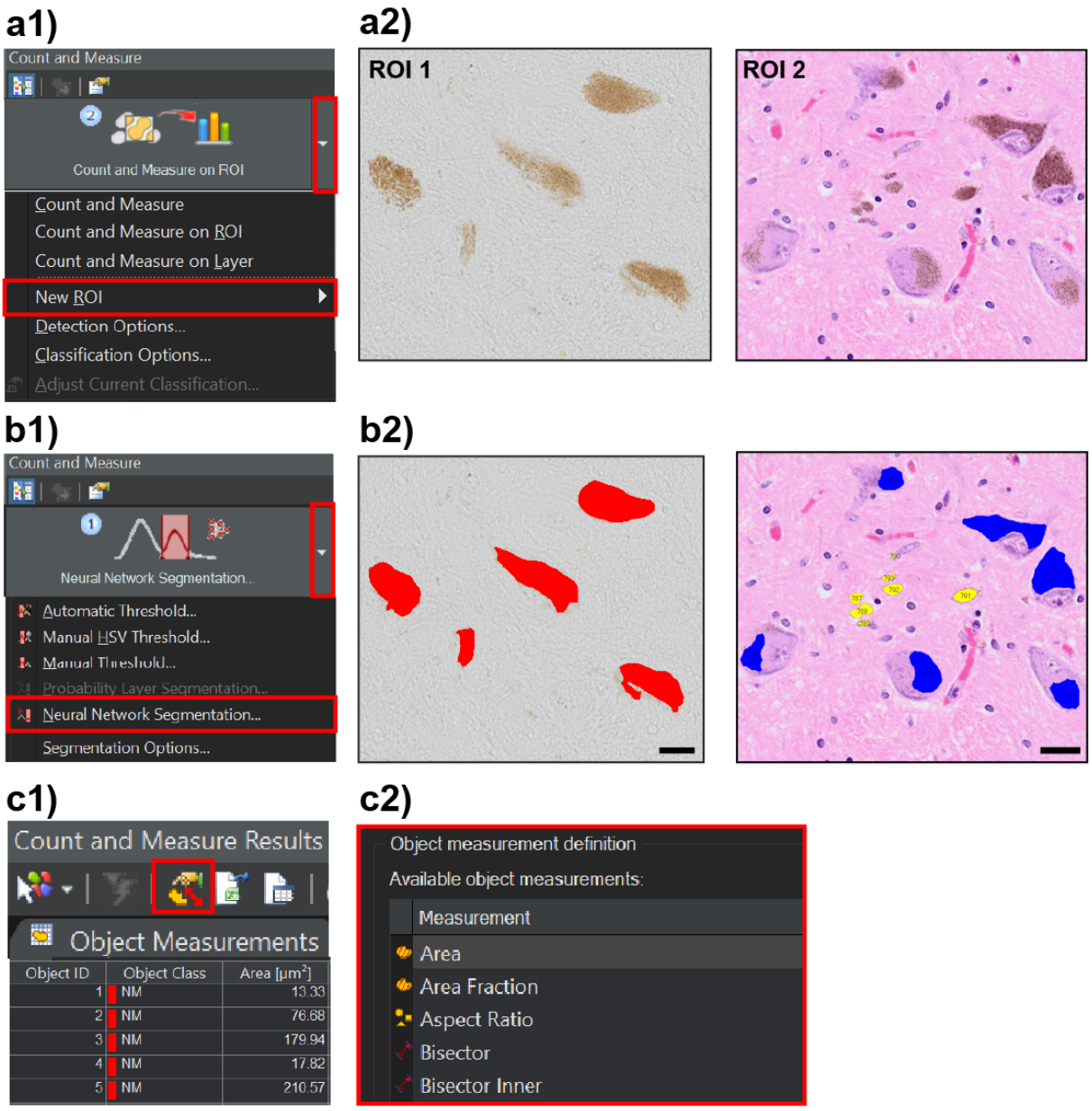

Figure 3 Automated TruAI quantification of neuromelanin. a1, a2) In selected sections, a new ROI needs to be drawn. b1, b2) The automated quantification of neuromelanin will run on the drawn ROI using the 'Neural Network Segmentation' option. Scale bars equal 20µm. c1, c2) A variety of features can be explored after completing neural network segmentation.

Statistical analysis

Statistical analyses were performed using R (R Project for Statistical Computing, RRID:SCR_001905, https://www.r-project.org/), IBM SPSS (SPSS Inc., Chicago, IL, USA, version 26, RRID:SCR_019096, https://www.ibm.com/products/spss-statistics) and GraphPad Prism (GraphPad Software Inc., California, USA, version 10.0.3, RRID:SCR_002798, http://www.graphpad.com/) statistical analysis software. Statistical significance was set at $P <$

0.05. For neuromelanin granule size thresholding, K-means clustering (k=2) was performed to determine size thresholds for intracellular versus extracellular neuromelanin. Scripts used for the analysis are available from https://doi.org/10.5281/zenodo.10494622. For intracellular neuromelanin, Mann-Whitney tests were performed to determine differences between stained and unstained sections in the area occupied by neuromelanin, the estimated grey optical density, and the colour intensity, with linear regression used to assess age related changes.

Results

The size of intracellular versus extracellular neuromelanin granules

Analysis of the size of iNM and eNM granules revealed that eNM granules were smaller than iNM granules. TruAI automated analysis was performed on unstained neuromelanin granules and their size examined in different substantia nigra pars compacta dopamine neuron subclusters including: the ventral tier (SNV), lateral part (SNL) and dorsal tier (SND). The distribution of neuromelanin granule size (log10) in SNV, SNL and SND revealed two distinct modes (Figure 4a). K-means clustering was performed to identify iNM and eNM size thresholds based on these two modes. The threshold for iNM granules was above 78.3μm^2, and the eNM granule cutoff was below 58.5μm^2 (Figure 4b). Scripts for this analysis are available from https://github.com/zchatt/Neuromelanin/tree/1.0.

This classification model was validated using H&E-stained sections. By using the iNM granule size threshold, we observed that nearly 70% of manually trained H&E-stained iNM granules fell within the threshold (Figure 4c, d). For eNM granules, we found that 90% of granules in all cases were smaller than 58.5 μm^2 (Figure 4e, f). The distributions were again bimodal and showed that the majority of eNM granules were very small in size compared with iNM granules.

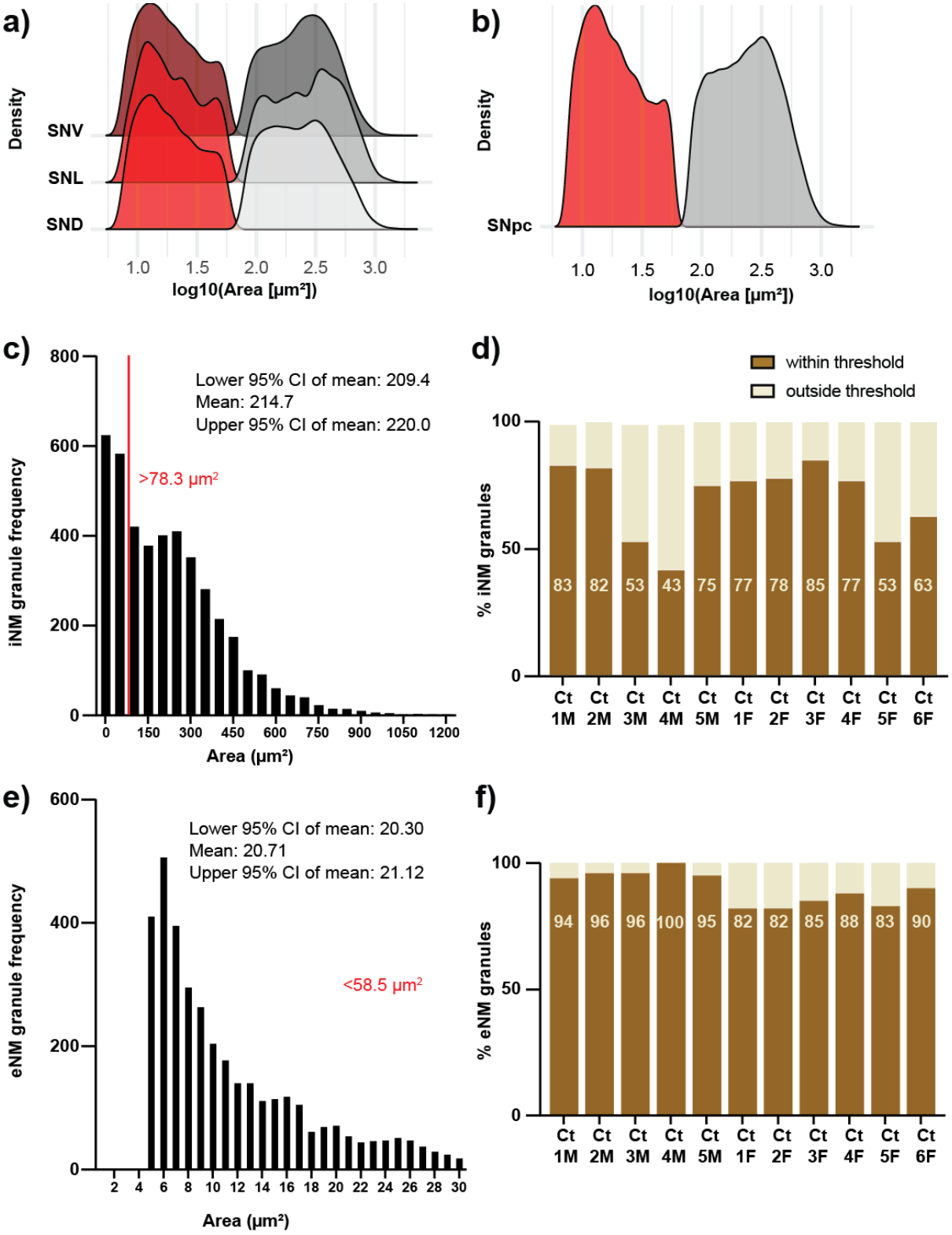

Figure 4 Neuromelanin size thresholding. a) Distribution of neuromelanin size (log10) measured in unstained sections of the substantia nigra pars compacta ventral tier (SNV), lateral part (SNL), and dorsal tier (SND). K-means clustering was performed in each subregion independently. This defined eNM as <58.5µm^2 (red histogram) and iNM as >78.3µm^2 (grey histogram). b) Combined neuromelanin granule size distribution across the substantia nigra pars compacta (SNpc). c) iNM size threshold applied to manually trained H&E stained iNM granules. The distribution of iNM size with respect to the defined threshold is shown. d) Proportion of manually trained H&E stained iNM granules included within the defined threshold. e) eNM area threshold applied to manually trained H&E stained eNM granules. f) Proportion of manually trained H&E stained eNM granules included within the threshold.

The intracellular area occupied by neuromelanin granules

While the intracellular area occupied by iNM granules did not appear to be different by eye (Figure 5a), unstained iNM granules occupied a significantly larger neuronal area compared to H&E stained granules (Figure 5b), potentially due to differences in tissue processing. While H&E stained iNM granules occupied a greater area of the neurons with increasing age, this relationship was lost when assessing the area occupied by the less processed unstained iNM with age (Figure 5c, d). These results reveal that histological processing impacts on the intracellular area occupied by iNM.

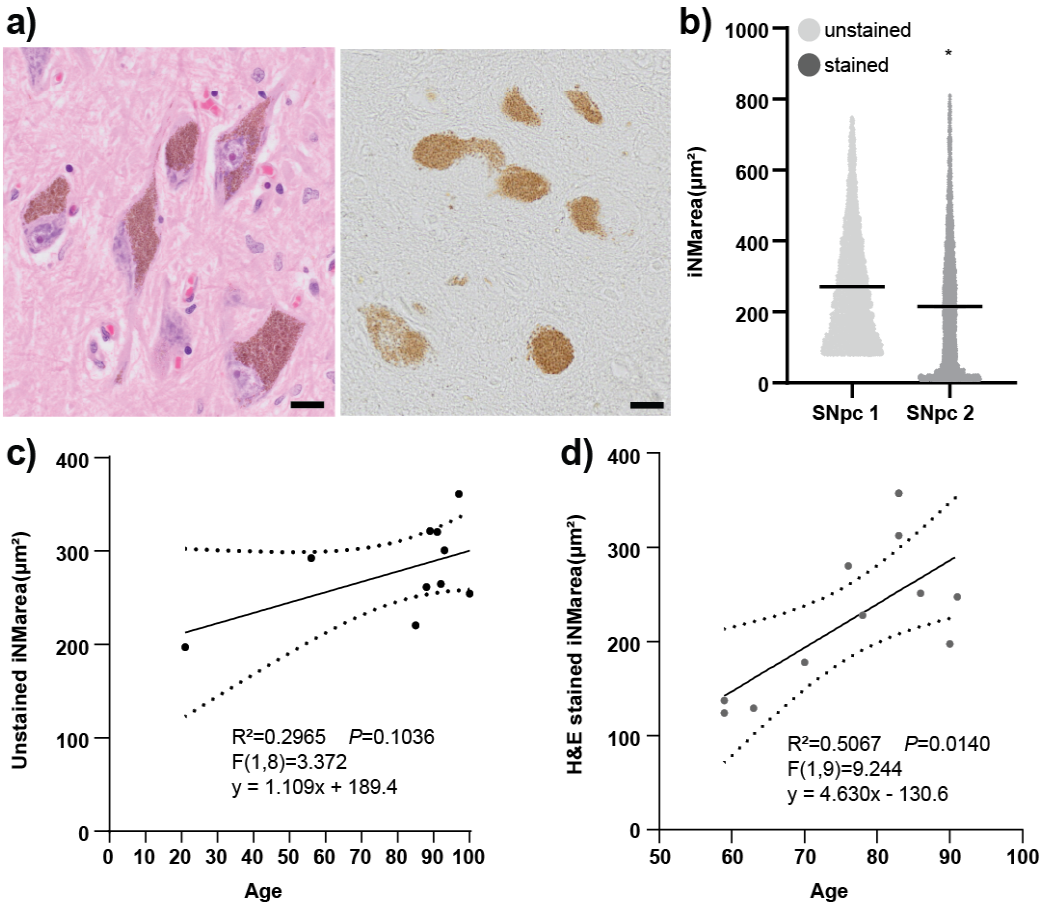

Figure 5 Analysis of the intracellular area occupied by neuromelanin. a) Representative images showing iNM granules in H&E-stained and unstained sections of the same regions of the substantia nigra pars compacta. Scale bars equal 20µm. b) Violin plots of the intracellular area occupied by intracellular neuromelanin granules (iNM) in the substantia nigra pars compacta (SNpc). The intracellular area occupied by unstained iNM was significantly larger than the intracellular area of H&E stained iNM, $P < 0.0001$, Mann-Whitney test. c, d) Scatterplots of the intracellular area occupied by unstained (c) versus H&E stained (d) iNM in healthy aging. There is an increase in the intracellular area occupied by iNM with increasing age which was significant in the H&E stained sections, linear regression $P < 0.05$.

The optical density of intracellular neuromelanin

The optical density of iNM can be determined by its grey intensity. This measurement captures iNM accumulation and compaction. In previously used software, this feature was automatically quantified as a greyscale parameter. However, the TruAI platform is more comprehensive because it shows individual red, green and blue pixel measurements. To compute the optical density of iNM, the standard weighted equation from the red, green and blue colour intensity measures were used to estimate greyscale intensity:

$$255 - (0.299 \times Mean\ (Red) + 0.587 \times Mean\ (Green) + 0.114 \times Mean\ (Blue))$$

The estimated greyscale intensity did not significantly differ between unstained and H&E stained iNM (supporting information Figure S3a). As expected, there is a significant increase in iNM estimated greyscale intensity with ageing (supporting information Figure S3b).

Colour analysis of intracellular neuromelanin

Different types of peripheral melanins have different colours, so the analysis of colour could indicate similarities to other types of melanins [15]. We conducted a novel iNM colour analysis using TruAI red, green and blue pixel intensities. Initially, we evaluated the mean red, green and blue colour in unstained and stained sections. Notably, red, green and blue mean colour intensities showed significant differences in unstained and stained iNM granules, with the H&E stained sections having more red and blue colour and less green colour ($P < 0.0001$ Mann-Whitney test, Figure 6a1-3).

To determine the individual colour contribution in iNM granules we calculated the weight of each red, green and blue colour using the following equation:

$$\frac{mean\ Red,\ Green,\ or\ Blue}{mean\ (Red\ +\ Green\ +\ Blue)} \times 100$$

The individual colour contributions were also significantly different ($P < 0.0001$ Mann-Whitney test, Figure 6b1-3). Consistent with the absolute intensity, there was significantly more blue and less green in H&E-stained iNM granules (Figure 6b2-3), but now slightly less red colour in the H&E-stained iNM granules compared to unstained granules (Figure 6b1). This data suggests that the hematoxylin contributes most to the colour change in iNM.

Given that combined red, green and blue greyscale intensity increased with age, we were interested in seeing if any individual colour contributed to this change over time. Green intensity was significantly reduced in both unstained and stained iNM granules, whereas blue was only significantly reduced in unstained sections (Figure 6c1-3, d1-3). In contrast, red intensity remained stable in iNM granules under both conditions.

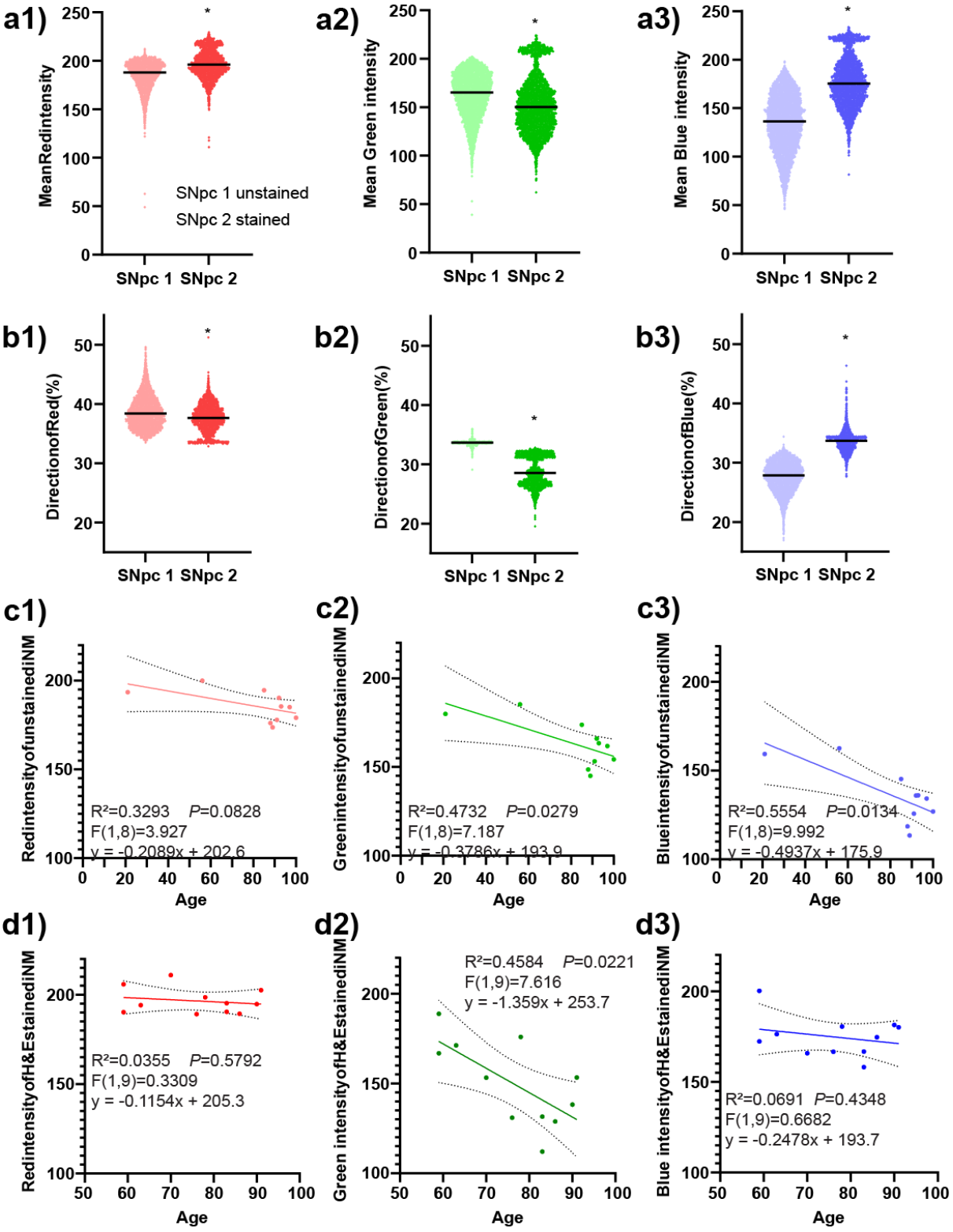

Figure 6 *Colour intensity of intracellular neuromelanin granules (iNM). a1, a2, a3) Violin plots of the mean red, green, and blue intensities in unstained and H&E stained iNM granules in the substanita nigra pars compacta (SNpc). The H&E stained sections had more red and blue iNM compared to unstained sections, P < 0.0001, Mann-Whitney test. b1, b2, b3) Violin plots of weighted average individual colour contribution to iNM granules in unstained and H&E stained sctions showing that blue contributes most to the change in iNM colour in H&E sections, P < 0.0001, Mann-Whitney test. c1, c2, c3) Simple linear regression of red, green and blue intensities in unstained iNM showing significant reductions in gren and blue intensity with*

age, P < 0.05. d1, d2, d3) Simple linear regression of red, green and blue intensities in H&E stained iNM showing that only the green intensity reduces with age, P < 0.05.

Discussion

The most vulnerable neurons to PD are those that make the largely human unique iNM. Understanding the role of neuromelanin in PD requires the standardization of analysis platforms. We developed and validated an automated quantification workflow for reproducibly analysing neuromelanin in human post-mortem tissue sections. The protocol was tested on both unstained and H&E-stained tissue samples, allowing for the differentiation of iNM and eNM granules. In unstained sections, the TruAI software was trained to detect pigments using deep learning, followed by k-means clustering to establish iNM and eNM granule size thresholds. In contrast, nuclear staining allowed for manual characterisation of iNM and eNM in H&E stained sections [16]. The system was then used to analyse parameters such as granule size, area occupied by iNM, optical density, and pigment colour. Our findings show that there is a substantial size difference between iNM and eNM, and that H&E staining affects the area occupied by iNM (through longer tissue processing).

Comparison of unstained versus stained neuromelanin granule size found two clusters in unstained sections when applying a k-means clustering size threshold. In H&E stained tissue sections, this threshold was less sensitive for iNM granules, with nearly half of the iNM being smaller than the threshold in some cases. This exclusion of smaller stained particles in cells in H&E sections can be attributed to the similar dense blue staining of other smaller organelles, like ribosomes and mitochondria, as well as more shrinkage of the sections during the staining process [17-19]. The increased susceptibility of iNM granules to tissue shrinkage is attributed to lipid loss during dehydration and clearing [20]. Lipid droplets are key components of iNM, and the removal of these structures contributes to granule shrinkage [12, 21, 22]. This is

supported by the observation that the iNM area was significantly smaller in H&E stained tissue sections neurons than unstained neurons. Despite these artifacts, unstained and H&E stained eNM was significantly smaller than the size of the iNM granules.

Histological processing also affected the intracellular area occupied by iNM. Consistent with previous findings, the intracellular area occupied by unstained iNM showed stability with increasing age [7]. However, the intracellular area occupied by H&E stained iNM significantly increased with age. This has also been shown previously with the suggestion that the elderly have less neurons, but that remaining neurons are larger in size with no substantial change in the total perikaryon volume [23]. If such an age-associated change is related to tissue processing rather than actual neuronal size, the increased shrinkage of younger versus older brain tissue could suggest significant tissue composition differences with age. Recent analyses show a decreased volume and increased iron content in the SNpc with age [22, 24-26], with the decreased volume potentially suggesting shrinkage over time and increased iron potentially buttressing cell structures. This suggests that cell structures, and particularly iNM granules, may be less prone to tissue processing shrinkage in older individuals. In healthy aging, NM granules sequester and store metals and cytotoxic quinones in lysosomes [22, 25, 26]. To maintain the stability of these pigments, lipid droplets support lysosomes through N-glycosylation [27]. Consequently, the older lipid droplets in iNM may exhibit chemical differences and be less susceptible to shrinkage during histological processing. In contrast, the estimated optical density showed the expected age-related linear increase [7], supporting the concept that increased iron may buttress the structure of older iNM. These measurements confirm the reliability of TruAI quantitation across differently stained tissue sections.

TruAI enabled new measurements of iNM, particularly color analysis that is thought to be of functional relevance. Peripheral melanin consists of brown-black eumelanin and red-yellow pheomelanin [15], which have different functions - eumelanin acts as an antioxidant whereas

pheomelanin is a pro-oxidant [28]. The standardized TruAI quantification method explored these colour features in nigral neuromelanin pigments with and without H&E staining. The levels of red, green, and blue varied between unstained and H&E stained iNM granules. H&E stained granules showed higher levels of blue, likely due to the blue-purple hematoxylin pigment used in the staining process. Despite these differences, red was the predominant color component in both types of iNM granules, indicating the presence of pheomelanin in healthy aging. However, since red is just one color, further evaluation of the combination of red, green and blue is needed.

Finally, we examined age-related colour changes. The red iNM component does not change with age, whereas green decreases significantly. Blue decreases significantly only in unstained iNM granules. In contrast, blue remained stable in H&E stained iNM granules, likely due to the presence of blue-purple hematoxylin pigment used in H&E staining that masks the true color change. These combined colour alterations may indicate an increase in the brown-black eumelanin component. According to the additive red, green and blue color model, vibrant red and green combine to form yellow, whereas a reduction in green intensity contributes to brown. The balance between yellow and brown pigmentation in peripheral melanin is controlled by differential gene expression in Drosophila. Specifically, a lighter-yellow peripheral pigmentation results from a mutation of yellow gene [29]. In wild-type Drosophila, this gene contributes to dark brown eumelanin formation [30, 31]. This suggests that the loss of yellow may be related to the upregulation of antioxidant eumelanin in iNM in healthy aging.

Overall, we have developed a standardized automated platform for the objective measurement of neuromelanin granules in tissue sections. iNM measurements were performed in two laboratories in different continents giving similar results despite different methods, showing that the automated platform is accurate, easy to implement and reproducible. The TruAI platform allowed the accurate and standardised measurement of small intracellular granules

that have been previously hard to measure and analyse. We found considerable differences in the size of iNM versus eNM granules and analysed the colour/type of these iNM granules with age showing a change in colour suggesting an increase in antioxidant eumelanin over time. Analysis of H&E stained iNM granules supports a change in tissue and iNM components with advancing age. This standardized platform can now be used to determine disease and other associated changes in iNM that decrease the ability of catecholaminergic neurons to maintain their neuromelanin content prior to their neurodegeneration.

Author contributions

Conceptualisation and study design: Anastasia Filimontseva, Thais Cuadros, Zac Chatterton, YuHong Fu, Miquel Vila and Glenda Halliday. Data acquisition: Anastasia Filimontseva, Thais Cuadros and Zac Chatterton. Data analysis and interpretation: Anastasia Filimontseva, Thais Cuadros, Zac Chatterton, YuHong Fu, Miquel Vila and Glenda Halliday. Reagent/materials/analysis tools: Anastasia Filimontseva, Thais Cuadros, Zac Chatterton, YuHong Fu, Miquel Vila and Glenda Halliday. Drafting of the manuscript: Anastasia Filimontseva, Thais Cuadros and Glenda Halliday. Editing of the manuscript: Anastasia Filimontseva, Thais Cuadros, Zac Chatterton, YuHong Fu, Miquel Vila and Glenda Halliday. All authors have read and approved the final manuscript.

References

1 Ono D, Dickson DW, Koga S. Evaluating the efficacy of few-shot learning for GPT-4Vision in neurodegenerative disease histopathology: A comparative analysis with convolutional neural network model. Neuropathol Appl Neurobiol 2024; 50: e12997

2 Gómez-de-Mariscal E, García-López-de-Haro C, Ouyang W, Donati L, Lundberg E, Unser M, Muñoz-Barrutia A, Sage D. DeepImageJ: A user-friendly environment to run deep learning models in ImageJ. Nature Methods 2021; 18: 1192-5
3 Kaczmarzyk JR, O'Callaghan A, Inglis F, Gat S, Kurc T, Gupta R, Bremer E, Bankhead P, Saltz JH. Open and reusable deep learning for pathology with WSInfer and QuPath. npj Precision Oncology 2024; 8: 9
4 Bankhead P, Loughrey MB, Fernández JA, Dombrowski Y, McArt DG, Dunne PD, McQuaid S, Gray RT, Murray LJ, Coleman HG, James JA, Salto-Tellez M, Hamilton PW. QuPath: Open source software for digital pathology image analysis. Scientific Reports 2017; 7: 16878
5 Courtney J-M, Morris GP, Cleary EM, Howells DW, Sutherland BA. Automated Quantification of Multiple Cell Types in Fluorescently Labeled Whole Mouse Brain Sections Using QuPath. Bio-protocol 2022; 12: e4459
6 Jo-Maree C, Gary PM, Elise MC, David WH, Brad AS. An Automated Approach to Improve the Quantification of Pericytes and Microglia in Whole Mouse Brain Sections. eneuro 2021; 8: ENEURO.0177-21.2021
7 Fedorow H, Halliday GM, Rickert CH, Gerlach M, Riederer P, Double KL. Evidence for specific phases in the development of human neuromelanin. Neurobiol Aging 2006; 27: 506-12
8 Hirsch E, Graybiel AM, Agid YA. Melanized dopaminergic neurons are differentially susceptible to degeneration in Parkinson's disease. Nature 1988; 334: 345-8
9 Huynh B, Fu Y, Kirik D, Shine JM, Halliday GM. Comparison of Locus Coeruleus Pathology with Nigral and Forebrain Pathology in Parkinson's Disease. Mov Disord 2021; 36: 2085-93
10 Hirsch EC, Graybiel AM, Agid Y. Selective vulnerability of pigmented dopaminergic neurons in Parkinson's disease. Acta Neurologica Scandinavica 1989; 80: 19-22
11 Faucheux BA, Martin ME, Beaumont C, Hauw JJ, Agid Y, Hirsch EC. Neuromelanin associated redox-active iron is increased in the substantia nigra of patients with Parkinson's disease. J Neurochem 2003; 86: 1142-8
12 Halliday GM, Ophof A, Broe M, Jensen PH, Kettle E, Fedorow H, Cartwright MI, Griffiths FM, Shepherd CE, Double KL. Alpha-synuclein redistributes to neuromelanin lipid in the substantia nigra early in Parkinson's disease. Brain 2005; 128: 2654-64
13 Carballo-Carbajal I, Laguna A, Romero-Giménez J, Cuadros T, Bové J, Martinez-Vicente M, Parent A, Gonzalez-Sepulveda M, Peñuelas N, Torra A, Rodríguez-Galván B, Ballabio

A, Hasegawa T, Bortolozzi A, Gelpi E, Vila M. Brain tyrosinase overexpression implicates age-dependent neuromelanin production in Parkinson's disease pathogenesis. Nature Communications 2019; 10: 973

14 Laguna A, Peñuelas N, Gonzalez-Sepulveda M, Nicolau A, Arthaud S, Guillard-Sirieix C, Lorente-Picón M, Compte J, Miquel-Rio L, Xicoy H, Liu J, Parent A, Cuadros T, Romero-Giménez J, Pujol G, Giménez-Llort L, Fort P, Bortolozzi A, Carballo-Carbajal I, Vila M. Modelling human neuronal catecholaminergic pigmentation in rodents recapitulates age-related neurodegenerative deficits. Nature Communications 2024; 15: 8819

15 Simon JD, Peles DN. The red and the black. Acc Chem Res 2010; 43: 1452-60

16 Korzhevskii DE, Kirik OV, Guselnikova VV, Tsyba DL, Fedorova EA, Grigorev IP. Changes in cytoplasmic and extracellular neuromelanin in human substantia nigra with normal aging. Eur J Histochem 2021; 65:

17 Bucher D, Scholz M, Stetter M, Obermayer K, Pflüger HJ. Correction methods for three-dimensional reconstructions from confocal images: I. Tissue shrinking and axial scaling. J Neurosci Methods 2000; 100: 135-43

18 Eisenberg BR, Mobley BA. Size changes in single muscle fibers during fixation and embedding. Tissue and Cell 1975; 7: 383-7

19 Rodgers G, Kuo W, Schulz G, Scheel M, Migga A, Bikis C, Tanner C, Kurtcuoglu V, Weitkamp T, Müller B. Virtual histology of an entire mouse brain from formalin fixation to paraffin embedding. Part 1: Data acquisition, anatomical feature segmentation, tracking global volume and density changes. Journal of Neuroscience Methods 2021; 364: 109354

20 Leist DP, Nettleton GS, Feldhoff RC. Determination of lipid loss during aqueous and phase partition fixation using formalin and glutaraldehyde. J Histochem Cytochem 1986; 34: 437-41

21 Sulzer D, Cassidy C, Horga G, Kang UJ, Fahn S, Casella L, Pezzoli G, Langley J, Hu XP, Zucca FA, Isaias IU, Zecca L. Neuromelanin detection by magnetic resonance imaging (MRI) and its promise as a biomarker for Parkinson's disease. npj Parkinson's Disease 2018; 4: 11

22 Zucca FA, Vanna R, Cupaioli FA, Bellei C, De Palma A, Di Silvestre D, Mauri P, Grassi S, Prinetti A, Casella L, Sulzer D, Zecca L. Neuromelanin organelles are specialized autolysosomes that accumulate undegraded proteins and lipids in aging human brain and are likely involved in Parkinson's disease. npj Parkinson's Disease 2018; 4: 17

23 Cabello CR, Thune JJ, Pakkenberg H, Pakkenberg B. Ageing of substantia nigra in humans: cell loss may be compensated by hypertrophy. Neuropathol Appl Neurobiol 2002; 28: 283-91

24 Li Y, Sethi SK, Zhang C, Miao Y, Yerramsetty KK, Palutla VK, Gharabaghi S, Wang C, He N, Cheng J, Yan F, Haacke EM. Iron Content in Deep Gray Matter as a Function of Age Using Quantitative Susceptibility Mapping: A Multicenter Study. Front Neurosci 2020; 14: 607705

25 Zecca L, Casella L, Albertini A, Bellei C, Zucca FA, Engelen M, Zadlo A, Szewczyk G, Zareba M, Sarna T. Neuromelanin can protect against iron-mediated oxidative damage in system modeling iron overload of brain aging and Parkinson's disease. Journal of Neurochemistry 2008; 106: 1866-75

26 Zecca L, Stroppolo A, Gatti A, Tampellini D, Toscani M, Gallorini M, Giaveri G, Arosio P, Santambrogio P, Fariello RG, Karatekin E, Kleinman MH, Turro N, Hornykiewicz O, Zucca FA. The role of iron and copper molecules in the neuronal vulnerability of locus coeruleus and substantia nigra during aging. Proc Natl Acad Sci U S A 2004; 101: 9843-8

27 Kundra R, Kornfeld S. Asparagine-linked oligosaccharides protect Lamp-1 and Lamp-2 from intracellular proteolysis. J Biol Chem 1999; 274: 31039-46

28 Kim E, Panzella L, Micillo R, Bentley WE, Napolitano A, Payne GF. Reverse Engineering Applied to Red Human Hair Pheomelanin Reveals Redox-Buffering as a Pro-Oxidant Mechanism. Scientific Reports 2015; 5: 18447

29 Wittkopp PJ, True JR, Carroll SB. Reciprocal functions of the Drosophila yellow and ebony proteins in the development and evolution of pigment patterns. Development 2002; 129: 1849-58

30 Barek H, Zhao H, Heath K, Veraksa A, Sugumaran M. Drosophila yellow-h encodes dopaminechrome tautomerase: A new enzyme in the eumelanin biosynthetic pathway. Pigment Cell & Melanoma Research 2022; 35: 26-37

31 Riedel F, Vorkel D, Eaton S. Megalin-dependent yellow endocytosis restricts melanization in the Drosophila cuticle. Development 2011; 138: 149-58